Molecular dynamics and density functional theory studies of substrate binding and catalysis of human brain aspartoacylase

Cheng-hua Zhang [a], Jie-Ying Gao [a], Ze-qin Chen [a], Ying Xue [a,b,*]

[a] College of Chemistry, Key Laboratory of Green Chemistry and Technology in Ministry of Education, Sichuan University, Chengdu 610064, PR China
[b] State Key Laboratory of Biotherapy, Sichuan University, Chengdu 610041, PR China

ABSTRACT

The active-site dynamics of human brain aspartoacylase (hASPA) complexed with its substrate (N-acetyl-ʟ-aspartate) has been studied using a hybrid quantum mechanical/molecular mechanical (QM/MM) approach based on the self-consistent charge-density functional tight-binding (SCC-DFTB) model. The Michaelis complex, which is constructed from a recent X-ray structure of the human brain aspartoacylase with a stable tetrahedral intermediate analogue, is reproduced in 1 ns molecular dynamics simulations at 300 K. The simulation shows that the substrate is tightly held in the active site by a hydrogen bond network and the putative nucleophilic water molecule is reasonably close to the nucleophilic center. the catalysis is further modeled with the density functional theory (DFT) in a truncated active-site model at the B3LYP/6-31G(d) level of theory. The DFT calculations indicate the reaction proceeds via a water promoted pathway with Glu178 serving as the general base and general acid. Transition state stabilization for nucleophilic addition is achieved by formations of the weak coordination bond between the substrate carbonyl oxygen atom and the zinc ion as well as of the strong hydrogen bonds between the substrate carbonyl oxygen atom and Arg63.

© 2010 Elsevier Inc. All rights reserved.

1. Introduction

Aspartoacylase (ASPA) catalyzes the deacetylation of N-acetyl-ʟ-aspartate (NAA), producing aspartate and acetate (Scheme 1). NAA, one of the most abundant amino acids in the brain [1], is synthesized from ʟ-aspartate and acetyl-CoA in the neuronal mitochondria of brain gray matter [2], and is released from neurons to the cerebrospinal fluid and then transported to oligodendrocytes [3,4]. Deficiency in ASPA is the established cause of Canavan disease (CD), which is a fatal autosomal-recessive disorder that affects the central nervous system, characterized by dysmyelination and spongiform degeneration of white matter in children [2,5–7]. There are more than 50 mutations in ASPA, including numerous deletions, missense mutations, and premature terminations, by analysis of the acy2 gene that encodes ASPA taken from DNA isolated from CD patients [8].

ASPA was primarily found in oligodendrocytes of white matter [9], and was originally proposed to be a member of the esterase family by means of a catalytic Ser-His-Glu triad [10]. However, subsequent alignment studies showed few similarities between ASPA and the esterase family. The recent sequence analyses have suggested that this enzyme belongs to the zinc–carboxypeptidase family [11], and is supported by recent work in which ASPA was shown to bind one zinc ion per monomer [12]. Recently, the crystal structures of the rat form and the human form of aspartoacylase have been determined at 1.8 and 2.8 Å resolutions, respectively, by Bitto et al. [13]. These structures confirm the presence of zinc in the enzyme and the identity of the zinc binding ligands which had been proposed previously. In addition, the ligands that are potentially involved in substrate binding have been suggested through a comparison of the structure of ASPA with those of the carboxypeptidases. Moreover, the structure of human brain aspartoacylase (hASPA) has been determined in the complex with a stable tetrahedral intermediate analogue, N-phosphonomethyl-ʟ-aspartate, by Le Coq et al. [14]. They proposed that the deacetylation of NAA is a carboxypeptidase-type mechanism for the hydrolysis of the amide bond of the substrate, based on the highly ordered binding of that potent inhibitor (Scheme 2). But there has been no report on the structure of any Michaelis complexes involving an ASPA and its substrate.

The first X-ray structure of hASPA with the tetrahedral intermediate mimic [14] provided valuable insights into the mode of substrate binding in the active site of hASPA. Moreover, the hybrid QM/MM methods to investigate the substrate binding and

* Corresponding author at: College of Chemistry, Key Laboratory of Green Chemistry and Technology in Ministry of Education, Sichuan University, Chengdu 610064, China. Tel.: +86 28 85418330.
E-mail addresses: yxue@scu.edu.cn, yingxue_99@yahoo.com (Y. Xue).
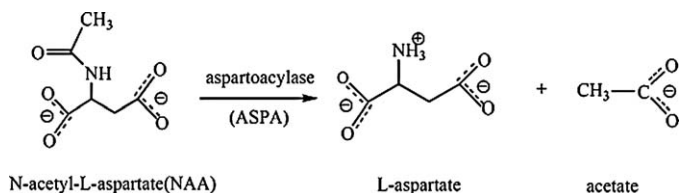
Scheme 1. Deacetylation of *N*-acetyl-L-aspartate (NAA) catalyzed by aspartoacylase (ASPA).

catalysis in metalloenzymes have been used everywhere [15–17]. The QM/MM approach is essential for it in principle offers a reliable description of both chemical and electrostatic interactions in the active site, such as polarization and charge transfer. However, such approaches are not without drawbacks. Chief among them is perhaps the steep scaling laws of the QM methods, especially for those based on first principles. The issue becomes critical for hASPA because of the necessarily large size of the QM region, which may include the metal ion, the protein ligands of the metal ion, the substrate, and the water/hydroxide nucleophile. Consequently, the QM model has to be very efficient to handle the simulations, particularly when the protein/solvent fluctuation needs be included.

In this work, we will take advantage of QM/MM simulation with an approximate density functional theory, the so-called self-consistent charge-density functional tight-binding (SCC-DFTB) model [18], to investigate the interaction between hASPA and its substrate. The SCC-DFTB method has been extensively tested [19–22] and applied successfully to several important enzymatic systems [23–26]. Here the QM/MM molecular dynamics (MD) studies the Michaelis complex of hASPA with its substrate NAA, which shed light on the active-site arrangement. Furthermore, we report a density functional theory (DFT) study of the catalysis with a truncated active-site model, which establishes the feasibility of the proposed reaction mechanism. Such a study is important for understanding the mode of substrate binding of hASPA and its catalytic deacylation mechanism.

2. Computational methods

2.1. QM/MM molecular dynamics simulations

The starting structure was based on the recently reported X-ray structure of hASPA complexed with the methylphosphonamidate inhibitor bound in the active site (PDB code 2O4H) [14]. The hASPA forms a dimer in the crystal structure, so it has two active sites and two corresponding inhibitors. In this study, we focus on the active site of the first monomer chain A. The substrate (NAA) was recovered by replacing the phosphorus atom of the inhibitor with the carbon atom, and the oxygen atom of the inhibitor within hydrogen bonding distance to the Glu178 side chain was modeled as the putative nucleophilic water. In all known Zn catalytic sites, a solvent species is always a Zn-ligand [27]. Then a very short steepest decent minimization of the substrate and the putative nucleophilic water molecule was performed to relax the system. Once the model enzyme–substrate (ES) complex was constructed, it was solvated by a pre-equilibrated sphere of TIP3P water molecules [28] with a 25 Å radius centered at the Zn atom. Any water molecule found within a 2.8 Å radius of a heavy protein/substrate atom was deleted, followed by relaxation of the solvent water sphere.

To reduce the computational cost, stochastic boundary conditions [29] were applied to the solvated system. The system is governed by Newtonian dynamics on a classical potential in the reaction region ($r < 22$ Å). The atoms in the reservoir zone outside the 25 Å radius were deleted. The atoms in the buffer zone (22 Å $< r <$ 25 Å) were simulated with the Langevin dynamics with friction and random forces stemmed from the bulk solvent that were not explicitly included in the simulation. The final size of the system contains 7713 atoms, including 19 substrate atoms and 763 water molecules.

The atoms in the MM region are governed by the CHARMM22 all-atom force field [30]. The QM region consists of 67 atoms, including the substrate, the putative nucleophilic water, and Zn atom as well as the side-chains of His21, Glu24, His116, and
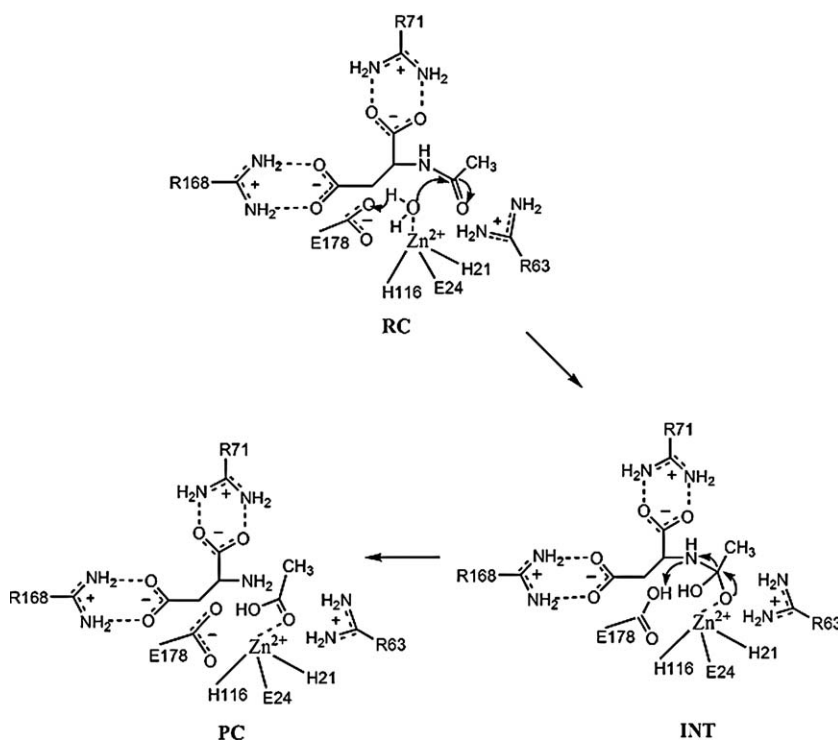
Scheme 2. Proposed mechanism of action of hASPA from Ref [14].

Glu178. The QM–MM interface was approximated by link atoms [31,32], which interact with all MM atoms except the link hosts. In this work, we have four link atoms connected with the C_β atoms of the corresponding protein residues with the C_α atoms as the link hosts. The CHARMM van der Waals parameters were used for all QM atoms. Nonbonded interactions were cut off at 12 Å, but the electrostatic interactions were dealt with using the extended electrostatics model of the group method [33], which has been shown to provide a balanced treatment of the QM–MM interactions [17].

The trajectories were propagated with a time step of 1 fs and the SHAKE algorithm [34] was applied to maintain the covalent bonds involving H atoms. All the calculations reported in this work were carried out by using the CHARMM suite of molecular simulation programs [35]. The MD simulation was performed for 1 ns after 100 ps of equilibration, in which the temperature was slowly brought to 300 K.

2.2. Truncated active-site model

A truncated active-site model based on the final QM/MM MD simulation as described in the previous section was constructed to investigate the reaction mechanism of the hASPA. It includes the substrate, the putative nucleophilic water molecule, the Glu178, the zinc ion and the three protein ligands of Zn(II). In addition, we have the side-chains of several key active-site residues (Arg63, Asn70, Arg71, and Arg168) in the model to simulate the binding mode of the substrate. To reduce computational costs, the arginine, glutamine, histidine, and the asparagine residues were approximated by methyl guanidine, acetate, methyl imidazole and acetamide, respectively. The total number of atoms is 109 and the total charge is +1.

The B3LYP exchange-correlation functional [36,37] and a standard basis set of 6-31G(d) were used in full geometry optimization of stationary points, followed by harmonic vibrational frequency calculations for confirmation. These stationary points were then connected by intrinsic reaction coordinate (IRC) method [38]. The solvent effects were studied with the PCM model [39] with dielectric constants of water ($\varepsilon = 80$) and protein ($\varepsilon = 5$). All of the computations were carried out using the Gaussian 03 suite of programs [40].

3. Results and discussions

3.1. Active-site dynamics of the ES complex

An 1 ns QM/MM MD simulations was performed for the ES complex. Fig. 1 shows the time evolutions of the root-mean-square deviation (RMSD) at 300 K of the backbone atoms of the simulated ES complex from the initial crystal structure, with averaged value of 0.90 ± 0.06 Å, indicating that the simulated structure was stable. The atomic numbering and important interactions at the active site of the hASPA-NAA complex are shown in Scheme 3. The averaged geometric parameters along the MD trajectory are listed in Table 1, along with available experimental data of hASPA complexed with the methylphosphonamidate inhibitor.

A snapshot of the active site of the ES complex is depicted in Fig. 2. From Fig. 2, we can see that the zinc ion is tetra-coordinated and the four ligands consist of the two histidine residues (His21 and His116), the glutamic acid (Glu24), and the putative nucleophilic water molecule. The distance of Zn–$O_{\varepsilon 1}$ (Glu24) is mostly reproduced well by the simulation, and was found in the simulation to be 2.12 ± 0.07 Å, comparable to the experimental distance of 2.15 Å [14], as shown in Table 1.

According to our model based on the X-ray structure, the substrate NAA forms an extensive network of interactions with
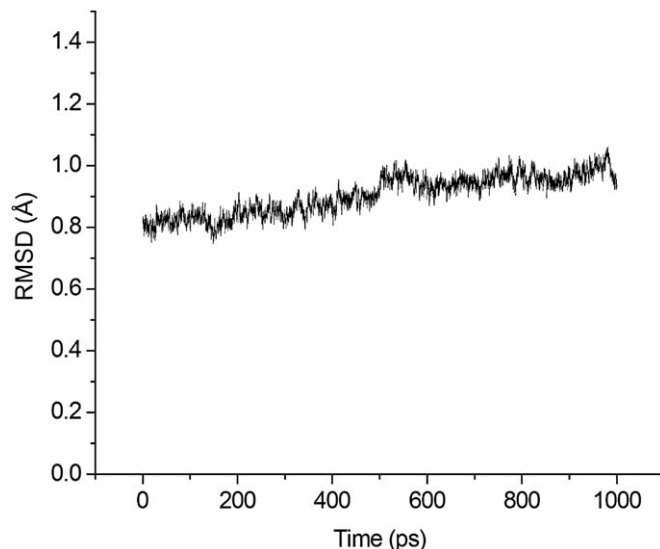
Fig. 1. RMSD of the backbone atoms of QM/MM MD simulated ES complex at 300 K from the crystal structure was plotted from 0 to 1000 ps.

many residues of the enzyme through its carbonyl oxygen, α-carboxylate, and β-carboxylate. From Scheme 3 and Table 1, one can see that the carbonyl oxygen forms the hydrogen bond with the guanidinium group of Arg63, as implied by the O_6–H_{11} (Arg63) distance of 1.88 ± 0.18 Å and O_6–H_{21} (Arg63) distance of 1.87 ± 0.20 Å. The α-carboxylate group forms a bidentate interaction with Arg71 in addition to interacting with Asn70 and Tyr288. The β-carboxylate of the substrate forms a bidentate interaction with Arg168. In our simulation, we also observed there is a hydrogen bond between the hydrogen atom of Asn70 and the β-carboxylic oxygen, as evidenced by the O_{41}–$H_{\delta 1}$ (Asn70) distance of 2.13 ± 0.33 Å.

As suggested by the X-ray structure, the side chain of Tyr164 is well positioned to bond with the β-carboxylate group of the intermediate analogue [14]. In our QM/MM MD simulation, the hydrogen bond between the hydroxyl hydrogen atom of Tyr164 and the β-carboxylic O_{42} atom was found to be 1.67 ± 0.10 Å. Throughout the MD simulation, the hydrogen bond is very stable, and the fluctuation of this hydrogen bond distance is given in Fig. 3.

The position and orientation of the putative nucleophilic water molecule are important factors in the preorganization of the near-attack configuration in the Michaelis complex. The putative

Table 1
Comparison of QM/MM MD simulations and experimental geometrical parameters for ES complex.

Distance (Å)	QM/MM MD	Exp[a]
O_w–C_6	2.66 ± 0.15	–
H_{w1}–$O_{\varepsilon 2}$ (Glu178)	1.60 ± 0.10	–
Zn–O_w	2.06 ± 0.07	–
Zn–O_6	3.98 ± 0.29	–
Zn–N_δ (His21)	2.02 ± 0.06	2.23
Zn–$O_{\varepsilon 1}$ (Glu24)	2.12 ± 0.07	2.15
Zn–N_δ (His116)	1.96 ± 0.05	2.29
O_6–H_{11} (Arg63)	1.88 ± 0.18 (2.80 ± 0.14)[b]	(2.84)[b]
O_6–H_{21} (Arg63)	1.87 ± 0.20 (2.78 ± 0.15)[b]	(3.00)[b]
O_{11}–$H_{\delta 2}$ (Asn70)	2.07 ± 0.46 (3.02 ± 0.39)[b]	(2.63)[b]
O_{11}–H_{11} (Arg71)	1.61 ± 0.08 (2.62 ± 0.07)[b]	(3.01)[b]
O_{12}–H_{21} (Arg71)	1.69 ± 0.10 (2.68 ± 0.09)[b]	(2.79)[b]
O_{12}–HO (Tyr288)	1.81 ± 0.31 (2.74 ± 0.27)[c]	(2.67)[c]
O_{41}–$H_{\delta 1}$ (Asn70)	2.13 ± 0.33 (2.88 ± 0.17)[b]	(4.05)[b]
O_{41}–H_{11} (Arg168)	1.66 ± 0.10 (2.66 ± 0.09)[b]	(3.26)[b]
O_{42}–H_{21} (Arg168)	1.75 ± 0.17 (2.74 ± 0.15)[b]	(2.94)[b]
O_{42}–HO (Tyr164)	1.67 ± 0.10 (2.64 ± 0.10)[c]	(2.93)[c]

[a] Taken from Ref. [14].
[b] Distances between heavy atoms (N–O) are given in parentheses.
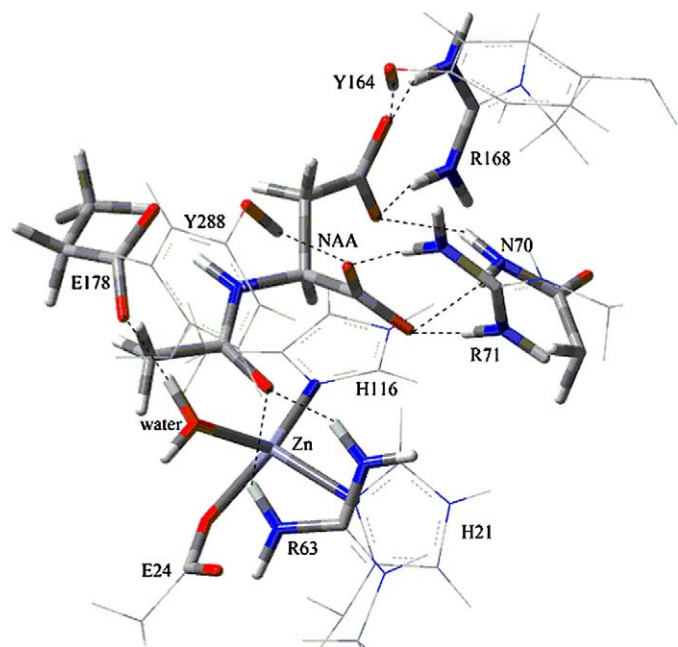[c] Distances between heavy atoms (O–O) are given in parentheses.
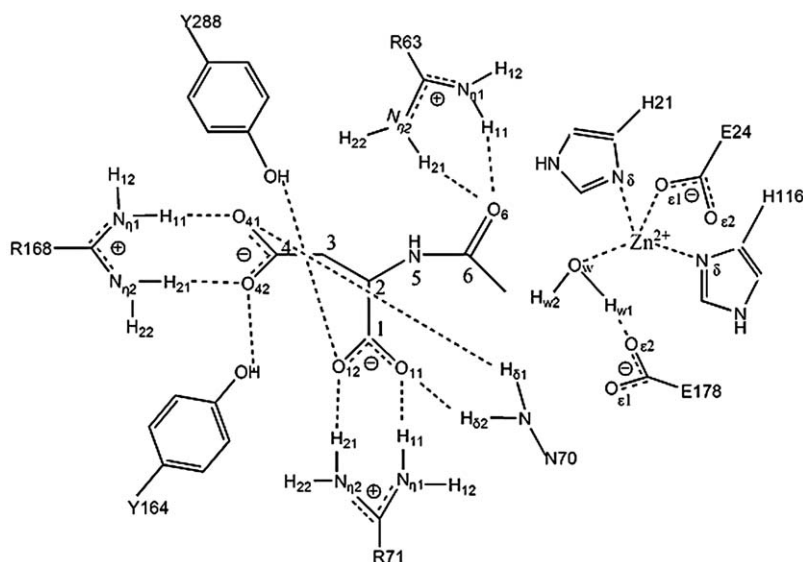
Scheme 3. Arrangement of active-site residues and their interactions with the substrate.

nucleophilic water molecule is well positioned for its nucleophilic attack of the carbonyl carbon (C_6) in the substrate. The O_w–C_6 distance was found to be 2.66 ± 0.15 Å in our simulation, as shown in Fig. 4. The orientation of the water is largely maintained by its hydrogen bond with Glu178, which is known to play a crucial role in catalysis of the deacylation of NAA. The length of strong hydrogen bond H_{w1}–$O_{\varepsilon2}$ (Glu178) was found to be 1.60 ± 0.10 Å, as also shown in Fig. 4. This hydrogen bond between the hydrogen atom of zinc-bound water and the side chain of Glu178 indicates that there maybe a proton transfer between them, then the hydrolysis reaction involves nucleophilic attack of the carbonyl carbon of the substrate by the formed zinc-coordinated hydroxyl group.
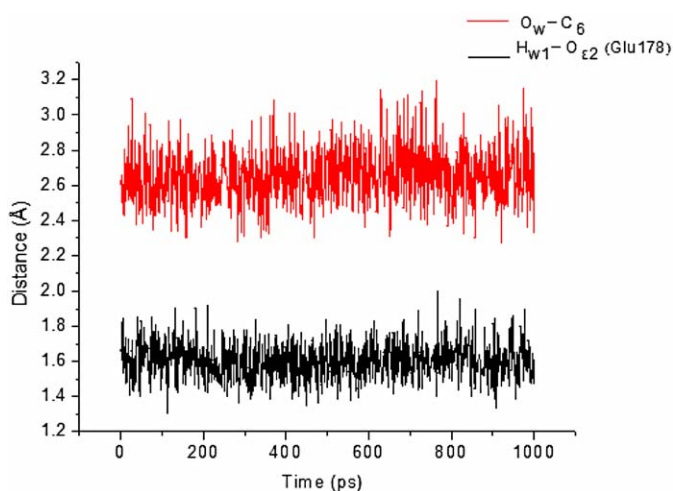
All of these features are in good agreement with the mechanism of the hydrolysis reaction proposed by Le Coq et al. [14] (see Scheme 2), in which the first step of NAA hydrolysis reaction catalyzed by hASPA involves nucleophilic attack of the carbonyl
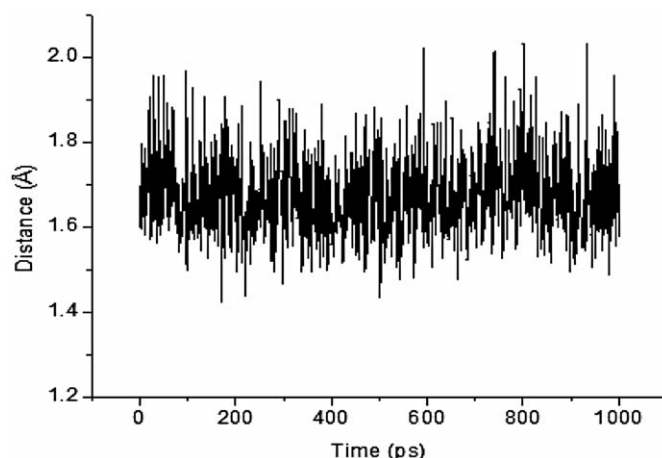
Fig. 3. Evolution of the hydrogen bond distances between the β-carboxylic O_{42} and the hydroxyl hydrogen atom of Tyr164.

Fig. 4. Evolution of the distance between the putative nucleophilic water molecule hydrogen (H_{w1}) and the oxygen ($O_{\varepsilon2}$) of Glu178 (black, bottom) in the ES complex and the distance between the nucleophilic water oxygen (O_w) and the substrate carbonyl carbon (C_6) (red, top). (For interpretation of the references to color in this figure legend, the reader is referred to the web version of the article.)

Fig. 2. Snapshot of the active site obtained from the QM/MM simulation of the ES complex.

carbon of the substrate by the zinc-coordinated hydroxyl group formed by proton transfer from the metal-bound water to Glu178. Hydroxide attack generates the tetrahedral intermediate and the developing negative charge on C=O group, which is stabilized by the positive charge on the guanidino group of Arg63. Our simulation shows that there is a strong hydrogen bond between H_{w1} and $O_{\epsilon2}$ (Glu178). Moreover, the distances of O_6–H_{11} (Arg63) and O_6–H_{21} (Arg63) in the Michaelis complex are 1.88 ± 0.18 and
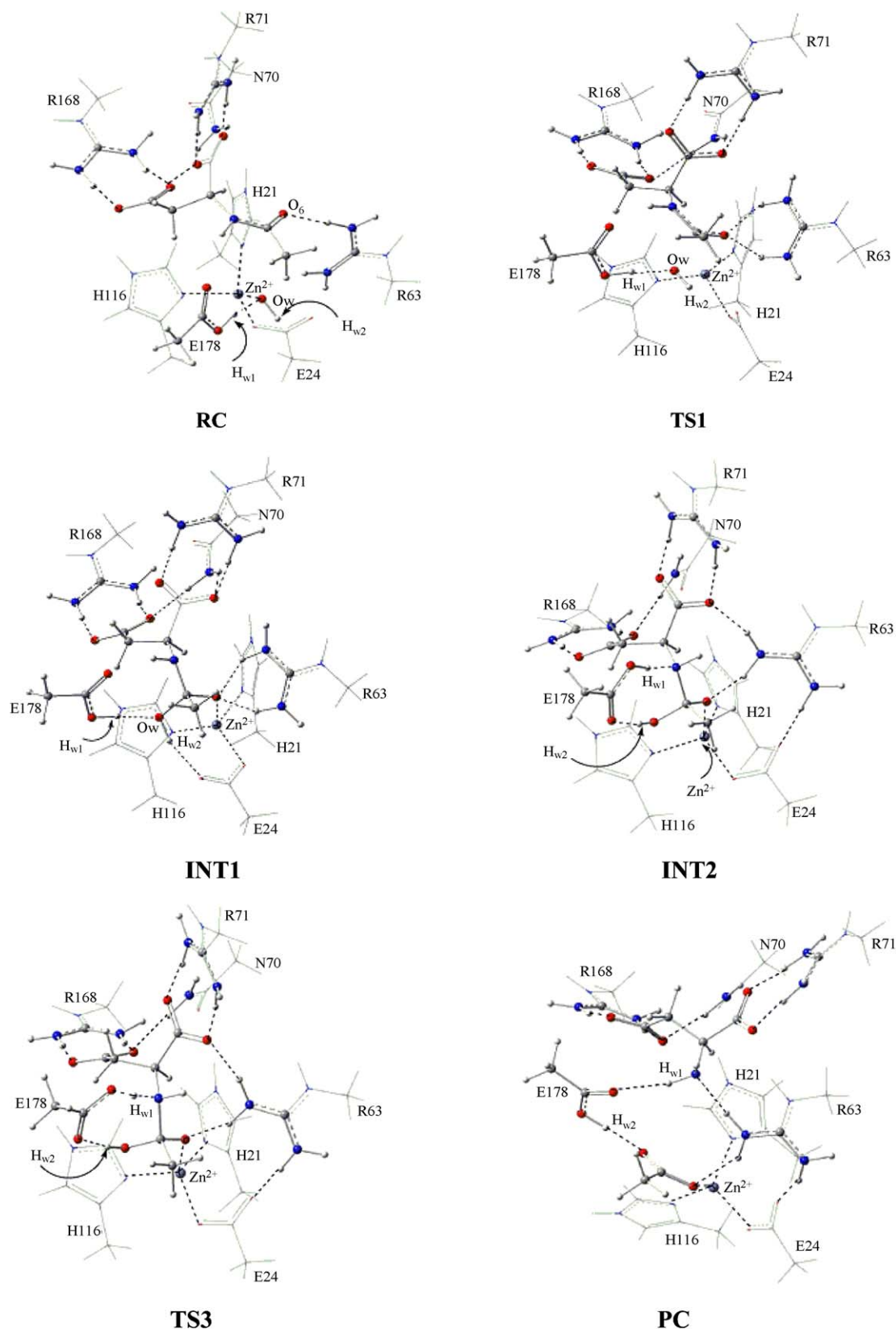

Fig. 5. Stationary point structures of the truncated active-site model obtained at the B3LYP/6-31G(d).

Table 2
Key geometric parameters of stationary points along the reaction path obtained at the B3LYP/6-31G(d) level of theory with the truncated active-site model.

Distance (Å)	Truncated active-site model					
	RC	TS1	INT1	INT2	TS3	PC
O_w–C_6	3.67	1.78	1.46	1.41	1.39	1.26
H_{w1}–$O_{\varepsilon2}$ (Glu178)	1.02	1.01	1.00	1.04	1.26	2.00
Zn–N_{δ}(His21)	2.04	2.09	2.06	2.05	2.04	2.01
Zn–$O_{\varepsilon1}$ (Glu24)	1.94	1.97	1.95	1.96	1.96	1.96
Zn–N_{δ}(His116)	2.03	2.08	2.04	2.05	2.05	2.06
Zn–O_w	1.95	2.12	2.90	2.99	3.03	3.06
Zn–O_6	4.72	2.15	1.97	1.94	1.95	1.96
O_6–H_{11} (Arg63)	2.94	1.78	1.76	3.47	3.59	3.95
O_6–H_{21} (Arg63)	1.76	1.85	1.84	1.68	1.72	2.14
O_{11}–$H_{\delta2}$ (Asn70)	1.98	2.04	2.10	3.81	3.89	4.22
O_{11}–H_{11} (Arg71)	1.66	1.67	1.67	1.68	1.70	1.67
O_{12}–H_{21} (Arg71)	1.63	1.59	1.58	1.65	1.68	1.65
O_{41}–$H_{\delta1}$ (Asn70)	1.86	1.92	1.87	1.81	1.82	1.80
O_{41}–H_{11} (Arg168)	1.72	1.76	1.71	1.67	1.67	1.68
O_{42}–H_{21} (Arg168)	1.77	1.67	1.75	1.74	1.74	1.71
C_6–O_6	1.25	1.33	1.39	1.37	1.36	1.28
C_6–N_5	1.34	1.38	1.44	1.52	1.55	4.10
H_{w1}–N_5				1.65	1.26	1.02

1.87 ± 0.20 Å, respectively. The zinc ion might also stabilize the developing negative charge in the tetrahedral intermediate. The C–N bond in the tetrahedral intermediate is then cleaved by protonation of the amino group by Glu178 to produce the acetate and L-aspartate products. Indeed, the active-site geometry of our model Michaelis complex provides a support to the proposed mechanism.

3.2. DFT studies of truncated active-site model

We have obtained six stationary points along the reaction path in the DFT investigations of the truncated active-site model at the B3LYP/6-31G(d) level. These stationary point structures and some key geometric parameters are listed in Fig. 5 and Table 2, respectively.

The geometry of the reactant complex (RC) in the truncated active-site model is very similar to that seen in our QM/MM MD simulations, featuring a tetra-coordinated Zn(II) and an intact amide C_6–N_5 bond in the substrate. The zinc-bound water shares one of its protons with the carboxylate group of Glu178. The Arg71, Arg168 and Asn70 interact with the carboxylate group of the substrate, the Arg63 binds to the carbonyl oxygen (O_6). The distance between the oxygen atom (O_w) of water and the carbonyl carbon (C_6) is 3.67 Å, comparable to the MD distance of 2.66 ± 0.15 Å. The distance of O_6–Zn bond is 4.72 Å in the RC, and the MD distance is 3.98 ± 0.29 Å, indicating the lack of direct interaction between the scissile carbonyl and the zinc ion in the ES complex.

As shown in Fig. 5, the rate-limiting transition state (TS1) features the nucleophilic addition (NA) of the zinc-bound water to the scissile carbonyl carbon (C_6) with the bond length of O_w–C_6 bond of 1.78 Å. From the RC through TS1 to the first tetrahedral intermediate (INT1), the O_6–Zn distance changes from 4.72 to 2.15 Å, finally to 1.97 Å, and the Arg63 forms hydrogen bonds with O_6, as evidenced by the O_6–H_{11} (Arg63) distance of 1.78 Å and the O_6–H_{21} (Arg63) distance of 1.85 Å at TS1. One can see that the

transition state stabilization for the NA step is achieved by formation of a weak coordination bond between the substrate carbonyl oxygen atom (O_6) and the zinc ion as well as of the strong hydrogen bonds between the O_6 and Arg63.

TS1 leads to the INT1 characterized by an sp^3 central carbon and a O_w–C_6 distance of 1.46 Å. The resulting negative charge on the O_6 is stabilized by the zinc ion as it replaces the water as the fourth ligand of Zn(II). So, the metal serves as a Lewis acid in catalysis. Then, the protonated carboxylate of Glu178 changes its conformation to form a hydrogen bond between the Glu178 proton (H_{w1}) and the backbone nitrogen (N_5), setting the stage for the elimination (E) step. Finally, The other transition state (TS3) is dominated by the proton transfer (PT) from the general base (protonated Glu178) to the nitrogen leaving group (N_5), leading to the cleavage of the amide C_6–N_5 bond. The sole imaginary frequency for the PT/E step is 794i cm^{-1}, indicating the strong involvement of PT.

The product complex (PC) has a cleaved peptide amide bond. In addition, the water ligand of the Zn(II) cofactor is replaced in PC by the substrate carbonyl oxygen (O_6), while the Glu178 carboxylate forms hydrogen bonds with the newly formed carboxylate group in the products.

The energies of the stationary points along the reaction path are listed in Table 3. As shown in Table 3, the inclusion of diffuse functions and polarization functions in the basis set did not qualitatively change the picture of the reaction path. The activation energy barrier is 34.3 kcal/mol, which decreases somewhat when solvation contributions were obtained using the PCM model, indicating an important role of the local solvation environment in the enzyme. Although several key residues have been included in the truncated active-site model, it might still be insufficient to correctly represent the enzymatic environment. It would be highly desirable to carry out quantum mechanical/molecular mechanical studies in order to elucidate how the enzyme catalyzes the reaction.

Table 3
Energetics of the stationary points along the reaction path with the truncated active-site model (energy in kcal/mol).

Methods	ES	TS1	INT1	INT2	TS3	EP
Energy (B3LYP/6-31G(d))	0.0	34.3	28.5	14.5	16.2	−17.0
Free energy (B3LYP/6-31G(d))	0.0	34.9	31.9	16.5	17.0	−14.9
PCM (B3LYP/6-31G(d) $w/\varepsilon = 80$)	0.0	26.1	23.0	15.4	14.0	−14.8
PCM (B3LYP/6-31G(d) $w/\varepsilon = 5$)	0.0	28.8	24.9	14.8	14.2	−15.6
Energy (B3LYP/6-31 + G(d,p)//B3LYP/6-31G(d))	0.0	38.0	32.8	16.4	17.7	−12.3

Interestingly, the tetrahedral intermediate (INT2) correlating with TS3 is somewhat different from INT1, due to a conformational change of the Glu178 carboxylate, which allows the formation of a hydrogen bond between the Glu178 proton and the backbone nitrogen (N_5). The energy of INT2 is lower than that of INT1 by 14.0 kcal/mol, due to the additional hydrogen bond between the $O_{\varepsilon 1}$ atom of Glu178 and the H_{w2} atom of the nucleophilic hydroxide. Unfortunately, the transition state between INT1 and INT2 was not found despite many attempts, but there is little reason to believe that this elusive transition state is rate-limiting.

4. Conclusion

In this work, we have used the QM/MM MD simulations to investigate the active-site dynamics of the hASPA complexed with its substrate NAA. The results reported here revealed a well organized active site of hASPA. The extensive network of interactions between the substrate and the active-site residues holds the substrate in the active site, which provided some important clues on the mode of substrate binding. The metal cofactor zinc is coordinated by His21, Glu24, His116, and the putative nucleophilic water molecule. This water molecule is not only reasonably close to the nucleophilic center, namely the carbonyl carbon of the substrate, but also oriented by a strong hydrogen bond to Glu178. It can easily form a hydroxyl group by transferring its proton to Glu178, which serves as a general base to activate the zinc-bound water. The geometry of the substrate in the Michaelis complex supports the proposed mechanism.

These structural determinants for the enzymatic reaction are confirmed by the DFT reaction path, which features that the Glu178 serves as the general base to facilitate the nucleophilic attack of the substrate carbonyl carbon by the deprotonated water nucleophile. Then Glu178 acts as a general acid to donate a proton to the amide nitrogen, leading to the cleavage of the peptide C–N bond. We believe that this mechanism should hold for the enzymatic system as well, but more detailed quantum mechanical/molecular mechanical studies are needed to confirm this hypothesis.

Acknowledgments

References

[1] H.H. Tallan, S. Moore, W.H. Stein, N-acetyl-L-aspartic acid in brain, J. Biol. Chem. 219 (1956) 257–264.
[2] C.N. Madhavarao, C. Chinopoulos, K. Chandrasekaran, M.A.A. Namboodiri, Characterization of the N-acetylaspartate biosynthetic enzyme from rat brain, J. Neurochem. 86 (2003) 824–835.
[3] W. Huang, H. Wang, R. Kekuda, Y.J. Fei, A. Friedrich, J. Wang, S.J. Conway, R.S. Cameron, F.H. Leibach, V. Ganapathy, Transport of N-acetylaspartate by the Na⁺-dependent high-affinity dicarboxylate transporter NaDC3 and its relevance to the expression of the transporter in the brain, J. Pharmacol. Exp. Ther. 295 (2000) 392–403.
[4] T.N. Sager, C. Thomsen, J.S. Valsborg, H. Laursen, A.J. Hansen, Astroglia contain a specific transport mechanism for N-acetyl-L-aspartate, J. Neurochem. 73 (1999) 807–811.
[5] R. Matalon, K. Michals, D. Sebesta, M. Deanching, P. Gashkoff, J. Casanova, Aspartoacylase deficiency and N-acctylaspartic aciduria in patients with Canavan disease, Am. J. Med. Genet. 29 (1988) 463–471.
[6] R. Matalon, K. Michals, R. Kaul, Canavan disease: from spongy degeneration to molecular analysis, J. Pediatr. 127 (1995) 511–517.
[7] R. Matalon, K. Michals-Matalon, Biochemistry and molecular biology of Canavan disease, Neurochem. Res. 24 (1999) 507–513.
[8] R. Matalon, K. Michals-Matalon, Recent advances in Canavan disease, Adv. Pediatr. 46 (1999) 493–506.
[9] C.N. Madhavarao, J.R. Moffett, R.A. Moore, R.E. Viola, M.A. Namboodiri, D.M. Jacobowitz, Immunohistochemical localization of aspartoacylase in the rat central nervous system, J. Comp. Neurol. 472 (2004) 318–329.
[10] R. Kaul, G.P. Gao, K. Balamurugan, R. Matalon, Human aspartoacylase cDNA and missense mutation in Canavan disease, Nat. Genet. 5 (1993) 118–123.
[11] K.S. Makarova, N.V. Grishin, The Zn-peptidase superfamily: functional convergence after evolutionary divergence, J. Mol. Biol. 292 (1999) 11–17.
[12] J. Le Coq, H.J. An, C. Lebrilla, R.E. Viola, Characterization of human aspartoacylase: the brain enzyme responsible for Canavan disease, Biochemistry 45 (2006) 5878–5884.
[13] E. Bitto, C.A. Bingman, G.E. Wesenberg, J.G. McCoy, G.N. Phillips Jr., Structure of aspartoacylase, the brain enzyme impaired in Canavan disease, Proc. Natl. Acad. Sci. U.S.A. 104 (2007) 456–461.
[14] J. Le Coq, A. Pavlovsky, R. Malik, R. Sanishvili, C. Xu, R.E. Viola, Examination of the mechanism of human brain aspartoacylase through the binding of an intermediate analogue, Biochemistry 47 (2008) 3484–3492.
[15] M.B. Peters, K. Raha, K.M. Merz, Quantum mechanics in structure-based drug design, Curr. Opin. Drug. Disc. Dev. 9 (2006) 370–379.
[16] A. Cavalli, P. Carloni, M. Recanatini, Target-related applications of first principles quantum chemical methods in drug design, Chem. Rev. 106 (2006) 3497–3519.
[17] D. Xu, H. Guo, Q. Cui, Antibiotic binding to dizinc β-lactamase L1 from steno-trophomonas maltophilia: SCC-DFTB/CHARMM and DFT studies, J. Phys. Chem. A 111 (2007) 5630–5636.
[18] M. Elstner, D. Porezag, G. Jungnickel, J. Elsner, M. Haugk, T. Frauenheim, S. Suhai, G. Seigert, Self-consistent-charge density-functional tight-binding method for simulations of complex materials properties, Phys. Rev. B 58 (1998) 7260–7268.
[19] Q. Cui, M. Elstner, E. Kaxiras, T. Frauenheim, M. Karplus, A QM/MM implementation of the self-consistent charge density functional tight binding (SCC-DFTB) method, J. Phys. Chem. B 105 (2001) 569–585.
[20] M. Elstner, P. Hobza, T. Frauenheim, S. Suhai, Hydrogen bonding and stacking interactions of nucleic acid base pairs: a density-functional-theory based treatment, J. Chem. Phys. 114 (2001) 5149–5155.
[21] J. Pu, J. Gao, D.G. Truhlar, Combining self-consistent-charge density-functional tight-binding (SCC-DFTB) with molecular mechanics by the generalized hybrid orbital (GHO) method, J. Phys. Chem. A 108 (2004) 5454–5463.
[22] H.A. Witek, K. Morokuma, Systematic study of vibrational frequencies calculated with the self-consistent charge density functional tight-binding method, J. Comput. Chem. 25 (2004) 1858–1864.
[23] Q. Cui, M. Elstner, M. Karplus, A theoretical analysis of the proton and hydride transfer in liver alcohol dehydrogenase (LADH), J. Phys. Chem. B 106 (2002) 2721–2740.
[24] M. Elstner, K.J. Jalkanen, M. Knapp-Mohammady, T. Frauenheim, S. Suhai, Energetics and structure of glycine and alanine based model peptides: approximate SCC-DFTB, AM1 and PM3 methods in comparison with DFT, HF and MP2 calculations, Chem. Phys. 263 (2001) 203–219.
[25] X. Zhang, D.H. Harrison, Q. Cui, Functional specificities of methylglyoxal synthase and triosephosphate isomerase: a combined QM/MM analysis, J. Am. Chem. Soc. 124 (2002) 14871–14878.
[26] H. Guo, N. Rao, Q. Xu, H. Guo, Origin of tight binding of a near-perfect transition-state analogue by cytidine deaminase: implications for enzyme catalysis, J. Am. Chem. Soc. 127 (2005) 3191–3197.
[27] D.S. Auld, Zinc coordination sphere in biochemical zinc sites, Biometals 14 (2001) 271–313.
[28] W.L. Jorgensen, J. Chandrasekhar, J.D. Madura, R.W. Impey, M.L. Klein, Comparison of simple potential functions for simulating liquid water, J. Chem. Phys. 79 (1983) 926–935.
[29] C.L. Brooks III, M. Karplus, Solvent effects on protein motion and protein effects on solvent motion: dynamics of the active site region of lysozyme, J. Mol. Biol. 208 (1989) 159–181.
[30] A.D. MacKerell Jr., D. Bashford, M. Bellott, R.L. Dunbrack Jr., J.D. Evanseck, M.J. Field, S. Fischer, J. Gao, H. Guo, S. Ha, D. Joseph-McCarthy, L. Kuchnir, K. Kuczera, F.T.K. Lau, C. Mattos, S. Michnick, T. Ngo, D.T. Nguyen, B. Prodhom, W.E. Reiher III, B. Roux, M. Schlenkrich, J.C. Smith, R. Stote, J. Straub, M. Watanabe, J. Wiorkie-wicz-Kuczera, D. Yin, M. Karplus, All-atom empirical potential for molecular modeling and dynamics studies of proteins, J. Phys. Chem. B 102 (1998) 3586–3616.
[31] A. Warshel, M. Levitt, Theoretical studies of enzymic reactions: dielectric, electrostatic and steric stabilization of the carbonium ion in the reaction of lysozyme, J. Mol. Biol. 103 (1976) 227–249.
[32] M.J. Field, P.A. Bash, M. Karplus, A combined quantum mechanical and molecular mechanical potential for molecular dynamics simulations, J. Comput. Chem. 11 (1990) 700–733.
[33] P.J. Steinbach, B.R. Brooks, New spherical-cutoff methods for long-range forces in macromolecular simulation, J. Comput. Chem. 15 (1994) 667–683.
[34] J.P. Ryckaert, G. Ciccotti, H.J.C. Berendsen, Numerical integration of the cartesian equations of motion of a system with constraints: molecular dynamics of n-alkanes, J. Comput. Phys. 23 (1977) 327–341.
[35] B.R. Brooks, R.E. Bruccoleri, B.D. Olafson, D.J. States, S. Swaminathan, M. Karplus, M. Charm, A program for macromolecular energy, minimization, and dynamics calculations, J. Comput. Chem. 4 (1983) 187–217.
[36] A.D. Becke, Density-functional thermochemistry. III. The role of exact exchange, J. Chem. Phys. 98 (1993) 5648–5652.
[37] C. Lee, W. Yang, R.G. Parr, Development of the Colle–Salvetti correlation-energy formula into a functional of the electron density, Phys. Rev. B 37 (1988) 785–789.
[38] C. Gonzalez, H.B. Schlegel, An improved algorithm for reaction path following, J. Chem. Phys. 90 (1989) 2154–2161.

[39] J. Tomasi, M. Persico, Molecular interactions in solution: an overview of methods based on continous distributions of the solvent, Chem. Rev. 94 (1994) 2027–2094.

[40] M.J. Frisch, G.W. Trucks, H.B. Schlegel, G.E. Scuseria, M.A. Robb, J.R. Cheeseman, J.A. Montgomery Jr., T. Vreven, K.N. Kudin, J.C. Burant, J.M. Millam, S.S. Iyengar, J. Tomasi, V. Barone, B. Mennucci, M. Cossi, G. Scalmani, N. Rega, G.A. Petersson, H. Nakatsuji, M. Hada, M. Ehara, K. Toyota, R. Fukuda, J. Hasegawa, M. Ishida, T. Nakajima, Y. Honda, O. Kitao, H. Nakai, M. Klene, X. Li, J.E. Knox, H.P. Hratchian, J.B. Cross, V. Bakken, C. Adamo, J. Jaramillo, R. Gomperts, R.E. Stratmann, O. Yazyev, A.J. Austin, R. Cammi, C. Pomelli, J.W. Ochterski, P.Y. Ayala, K. Morokuma, G.A. Voth, P. Salvador, J.J. Dannenberg, V.G. Zakrzewski, S. Dapprich, A.D. Daniels, M.C. Strain, O. Farkas, D.K. Malick, A.D. Rabuck, K. Raghavachari, J.B. Foresman, J.V. Ortiz, Q. Cui, A.G. Baboul, S. Clifford, J. Cioslowski, B.B. Stefanov, G. Liu, A. Liashenko, P. Piskorz, I. Komaromi, R.L. Martin, D.J. Fox, T. Keith, M.A. Al-Laham, C.Y. Peng, A. Nanayakkara, M. Challacombe, P.M.W. Gill, B. Johnson, W. Chen, M.W. Wong, C. Gonzalez, J.A. Pople, Gaussian 03, Revision D.01, Gaussian, Inc., Pittsburgh, PA, 2005.